Broadly neutralizing SARS-CoV-2 antibodies through epitope-based selection from convalescent patients

Romain Rouet[1,2*†], Jake Y. Henry[1,2†], Matt D. Johansen[3†], Meghna Sobti[2,4†], Harikrishnan Balachandran[5,6], David B. Langley[1,2], Gregory Walker[567], Helen Lenthall[1,2], Jennifer Jackson[1,2], Stephanie Ubiparipovic[1,2], Ohan Mazigi[1,2], Peter Schofield[1,2], Deborah L. Burnett[1,2], Simon H. J. Brown[8], Marianne Martinello[5,6], Bernard Hudson[9], Nicole Gilroy[10], Jeffrey J. Post[7], Anthony Kelleher[5,6], Hans-Martin Jäck[11], Christopher C. Goodnow[1,2], Stuart G. Turville[5,6], William D. Rawlinson[5,7], Rowena A. Bull[5,6‡], Alastair G. Stewart[2,4‡], Philip M. Hansbro[7‡] and Daniel Christ[1,2*‡]

[1]Garvan Institute of Medical Research, Sydney NSW, Australia

[2]UNSW Sydney, St Vincent's Clinical School, Faculty of Medicine, Sydney NSW, Australia

[3]Center for Inflammation, Centenary Institute and University of Technology Sydney, Sydney NSW, Australia

[4]Victor Chang Cardiac Research Institute, Sydney NSW, Australia

[5]UNSW Sydney, School of Medical Sciences, Faculty of Medicine, Sydney NSW, Australia

[6]Kirby Institute, UNSW Sydney, Sydney NSW, Australia

[7]Prince of Wales Hospital, Sydney NSW, Australia

[8]Molecular Horizons, University of Wollongong, Wollongong, NSW, Australia

[9]Royal North Shore Hospital, Sydney, NSW, Australia

[10]Westmead Hospital, Sydney, NSW, Australia

[11]Division of Molecular Immunology, Friedrich-Alexander University Erlangen-Nürnberg and University Hospital Erlangen, Erlangen-Nürnberg, Germany

* correspondence to Romain Rouet (r.rouet@garvan.org.au) and Daniel Christ (d.christ@garvan.org.au)

† equal contribution; ‡ senior authors

SUMMARY

Emerging variants of concern (VOCs) are threatening to limit the efficacy of SARS-CoV-2 monoclonal antibodies and vaccines currently used in clinical practice; broadly neutralizing antibodies and strategies for their identification are therefore urgently required. Here we demonstrate that broadly neutralizing antibodies can be isolated from peripheral blood mononuclear cells (PBMCs) of convalescent patients using SARS-CoV-2 receptor binding domains (RBDs) carrying epitope-specific mutations. This is exemplified by two human antibodies, GAR05, binding to epitope class 1, and GAR12, binding to a new epitope class 6 (located between class 3 and class 5). Both antibodies broadly neutralize VOCs, exceeding the potency of the clinical monoclonal sotrovimab (mAb S309) by orders of magnitude. They also provide potent prophylactic and therapeutic *in vivo* protection of hACE2 mice against viral challenge. Our results indicate that exposure to Wuhan SARS-CoV-2 induces antibodies that maintain potent and broad neutralization against emerging VOCs using two unique strategies: either by targeting the divergent class 1 epitope in a manner resistant to VOCs (ACE-2 mimicry, as illustrated by GAR05 and mAbs P2C-1F11/S2K14); or alternatively, by targeting rare and highly conserved epitopes, such as the new class 6 epitope identified here (as illustrated by GAR12). Our results provide guidance for next generation monoclonal antibody development and vaccine design.

52 **INTRODUCTION**

53 The coronavirus SARS-CoV-2, the causative agent of the global COVID-19 pandemic,
54 has resulted in the death of over 6 million people worldwide [1]. Upon SARS-CoV-2
55 infection, the human adaptive immune response generates antibodies against the viral
56 spike surface glycoprotein[2]. Most of the neutralizing antibodies bind the spike receptor
57 binding domain (RBD), and in particular class 1 and 2 epitopes within the receptor
58 binding motif (RBM), directly blocking interaction with the human angiotensin
59 converting enzyme receptor 2 (ACE2) [3-6]. Such RBD- and RBM-targeted antibodies
60 are also generated upon vaccination [7], but often lack neutralization potential against
61 emerging variants of concern (VOCs) [8-10]. More recently, broadly neutralizing
62 antibodies have been identified that bind outside the RBM region [11-15]. Such antibodies
63 generally bind to regions conserved among sarbecoviruses (class 3, 4 and 5 epitopes)
64 and are expected to be more resilient to VOCs. However, it is also evident that such
65 antibodies are rare in most vaccinated individuals and convalescent patients [5,14].
66
67 In addition to vaccination, the use of recombinant antibodies has proven successful for
68 therapy and prevention of COVID-19 and several monoclonal antibodies have obtained
69 regulatory approval [16-18]. However, increased resistance to antibody neutralization is
70 being observed for SARS-CoV-2 VOCs, especially for variants carrying mutations
71 within the RBM region (including Beta and Omicron variants) [8-10]. To overcome such
72 resistance, research has focused on the development of broadly neutralizing antibodies,
73 such as sotrovimab (S309), which targets the class 3 epitope, which is conserved in
74 sarbecoviruses [19]. In addition, antibody cocktails, targeting multiple non-overlapping
75 epitopes on the surface of the RBD have been developed to overcome resistance [20,21].
76

77 Here we outline a strategy based on the sorting of convalescent patient B cells in an
78 epitope-specific manner, in combination with structural characterization by X-ray
79 crystallography, cryo-electron microscopy (cryo-EM), live virus neutralization and
80 animal models. Using recombinant RBD proteins carrying epitope-specific mutations,
81 we identified neutralizing antibodies binding to diverse epitope classes. Our approach
82 identified a panel of three non-overlapping antibodies (GAR05, GAR12, and GAR20)
83 binding to epitopes classes 1, 6 and 4) that potently neutralize live virus *in vitro* and
84 protect K18-hACE2 mice from intranasal challenge. Although these monoclonals had
85 been isolated from convalescent patients infected early in the pandemic (Wuhan strain),
86 all three potently neutralized the immune evasive Delta VOC, with two of the three
87 (GAR05, GAR12) also potently neutralizing all analyzed Omicron subvariants,
88 highlighting the robustness of the approach. In addition to the previously described
89 class 1-5 epitopes of RBD, our work identified a new epitope class conserved in
90 sarbecoviruses, that we define as class 6, located between class 3 (exemplified by the
91 antibody S309 [19]) and class 5 (exemplified by the antibody S2H97[12]) epitopes. Taken
92 together, our approach identified new broadly neutralizing antibodies from
93 convalescent patients and outlined a new RBD epitope class (class 6), highlighting the
94 potential of the strategy for our understanding of the SARS-CoV-2 antibody response
95 and for future vaccine and therapeutic applications.
96
97 **RESULTS**
98 **Epitope-based selection of human memory B cells using mutant SARS-CoV-2**
99 **RBDs**
100 We utilized peripheral blood mononuclear cells (PBMCs) from convalescent patients
101 from the COSIN study (New South Wales COVID-19 patient cohort) [22], at 1- and 4-

102 months post SARS-CoV-2 infection. In order to rapidly identify antibodies binding to
103 different epitopes, we sorted memory B cells based on their capacity to bind to RBD
104 variants carrying epitope class-specific mutations. We initially investigated whether to
105 utilize full spike glycoprotein (trimeric; Wuhan strain [23]; randomly biotinylated) or
106 recombinant RBD (single biotin-tag) to select human memory B cells. Using
107 fluorescently-labeled tetramerized spike and tetramerized RBD, we observed a
108 population of $CD3^{-}CD19^{+}CD20^{+}CD10^{-}IgD^{-}IgG^{+}$ B cells with a high mean of
109 fluorescence intensity (MFI) for both the RBD and spike (albeit lower MFI for spike,
110 Fig. 1A and Supp. Fig. 1 - Sort 1). Subsequent sorting (Sort 2 and Sort 3; Fig 1A, Supp
111 Fig 1) focused on the use of tetramerized RBD and a series of SARS-CoV-2 RBD
112 mutants to target different epitope classes. We specifically designed RBD mutants to
113 differentiate antibodies blocking the ACE2 interactions and antibodies binding outside
114 the ACE2 binding site. For this purpose, we utilized the following mutant SARS-CoV-
115 2 RBDs: Mut1 (T500A/N501A/Y505A), perturbing the ACE2 binding site (targeting
116 class 1 and 2 antibody binders); Mut2 (L455A/F456A), blocking a different surface of
117 the ACE2 binding site (further targeting further class 1 and 2 binders); and Mut3
118 (K378S), blocking the CR3022 antibody epitope (targeting class 4 binders) (Fig. 1B)
119 [24]. In addition to mutants RBDs, we also utilized SARS-CoV-1 RBD in order to identify
120 broadly neutralizing antibodies (all RBDs were tetramerized with four distinct
121 fluorescent dyes (Supp. Fig. 1B)). Having observed RBD/spike cross-specificity (Sort
122 1), the next strategy (Sort 2) employed SARS-CoV-1, SARS-CoV-2 and Mut1 and
123 Mut3 RBDs, classifying cells as falling into class 1/2, 4 or unknown epitope classes
124 (Fig 1 and Supp Fig 1). We consolidated these findings using a third sorting strategy
125 (Sort 3) employing WT SARS-CoV-2, Mut1, Mut2 and Mut3 (Fig. 1A and Supp. Fig.
126 1 – Sort 3), strengthening delineation of binders that compete with the ACE2 interface.

127

128 **Epitope binning and characterization of human monoclonal antibodies**

129 Following the indexed sorting strategies, human antibody variable regions were
130 amplified from isolated B lymphocytes, cloned into human IgG1 expression vectors,
131 and the encoded monoclonal antibodies expressed and purified [25,26]. For an initial
132 screen, we assessed antibody binding by ELISA and found that 80% (16/20) of the
133 antibodies selected bound to WT SARS-CoV-2 RBD (Supp. Fig. 2A). We then
134 measured the antibody binding affinities to SARS-CoV-2 RBD by BioLayer
135 Interferometry (BLI), which ranged from 290 nM to 200 pM (Fig. 1C and Supp. Fig.
136 2B).

137

138 To further validate class 1/2 antibodies, we performed BLI competition assays with
139 recombinant human ACE2. Amongst the 16 antibodies screened, we identified seven
140 that competed with ACE2 and thus could be considered as class 1/2 candidates
141 (GAR04, 05, 06, 07, 09, 15 and 20) (Supp. Fig. 3). All but one of these (GAR04) were
142 capable of binding the E484K RBD mutant (Supp. Fig. 3), a residue pivotal to the
143 binding mode of many class 2 binders [6], hence we tentatively assigned GAR04 as a
144 class 2 binder, while the other six antibodies were assigned as class 1 binders (Fig 1D).
145 IGHV3-53, IGHV1-2 and IGHV3-30 germlines have been commonly observed among
146 class 1 and class 2 SARS-CoV-2 binders[27] , and we also observed these germlines
147 among several of these selected clones (including GAR01, GAR04, and GAR15).

148

149 To further validate class 4 antibodies, we first investigated cross-reactivity with other
150 sarbecovirus RBDs, which are known to be relatively conserved within this epitope
151 (SARS-CoV-1, pangolin CoV and bat RaTG12-CoV) [12,13]. We performed BLI binding

152 experiments with these three sarbecovirus RBDs and identified seven cross-reactive
153 antibodies (GAR01, 03, 11, 13, 14, 16 and 20) (Supp. Fig. 4). BLI competition assays
154 performed on these cross-reactive antibodies with the class 4 monoclonal antibody
155 CR3022 [28,29](known to bind both SARS-CoV-1 and SARS-CoV-2), confirmed that all,
156 except GAR01 and GAR03, bind to the class 4 epitope (Supp. Fig. 3). In addition to
157 competing with CR3022, GAR20 also blocked binding of recombinant ACE2 to SARS-
158 CoV-2 RBD, as observed for antibody 3467 [14], however this was not observed for the
159 other class 4 antibodies.
160
161 The finding that GAR01 and GAR03 are broadly cross-specific and bind to epitopes
162 conserved in SARS-CoV-2, SARS-CoV-1, pangolin CoV and bat RaTG12-CoV (but
163 do not compete with ACE2 nor CR3022) indicate that these two antibodies may be rare
164 binders falling into the class 5 epitope bin. To investigate this hypothesis, we performed
165 BLI competition assays with the class 5 antibody S2H97 [12], and confirmed that binding
166 of both antibodies is indeed consistent with the class 5 classification (Supp. Fig. 3).
167
168 Overall, our epitope-binning strategy assigned most of the antibodies to established
169 class 1-5 epitope bins (Fig. 1C)[30]. In addition, antibodies originally sorted into unknown
170 epitope bins were further identified as falling either into epitope class 1/2 (unaffected
171 by T500A/N501A/Y505A and L455A/F456A RBD mutations) or alternately as falling
172 into a new epitope class (class 6, as below).
173
174 Next, we evaluated the capacity of these antibodies to neutralize live virus. We
175 observed that 12/16 of the monoclonal antibodies neutralized SARS-CoV-2 Wuhan
176 (D614G) strain with IC_{50}s ranging from 20 µg/ml to 12 ng/ml (Fig. 1C, Fig. 1D).

177 Several (6/16) antibodies also neutralized the Delta VOC (GAR05, GAR07, GAR09,
178 GAR12, GAR15 and GAR20) (Fig. 1E). Three of these antibodies, GAR05, GAR12
179 and GAR20, were particularly broad in their specificity and neutralized all analyzed
180 variants of concern, with GAR05 neutralizing with IC_{50}s ranging from 115 to 26 ng/ml,
181 and GAR12 and GAR20 neutralizing with IC_{50}s ranging from 255 to 128 ng/ml and 12
182 to 4 µg/ml respectively (Supp. Fig. 5).
183
184 **GAR05 is a broadly neutralizing class 1 antibody**
185 Based on its potent and broad neutralization potential, antibody GAR05 was further
186 characterized by cryo-EM and X-ray crystallography. For cryo-EM studies, GAR05
187 Fab was incubated with stabilized D614G Wuhan trimeric spike ("VFLIP") [31] at a 3:1
188 molar ratio. The complex was subsequently flash-frozen and examined using cryo-EM
189 (Supp. Fig. 6 and Supp Table 2). The cryo-EM map of GAR05 bound to trimeric spike
190 (Fig. 2A, Supp Table 2) shows three antibody Fabs bound to the RBD domains of the
191 trimeric spike, where all three RBDs are in the up conformation, consistent with its
192 classification as a class 1 antibody (similarly to what has been observed for antibody
193 C105 [32]). We also solved the crystal structure of GAR05 as a Fab fragment in complex
194 with SARS-CoV-2 RBD to 3.2 Å resolution (Fig 2B, Supp. Table 1), essentially
195 confirming the binding mode suggested by the cryo-EM map. GAR05 straddles the
196 middle of the saddle-like RBD surface known to interact with the ACE2 receptor (Fig.
197 2B). The antibody forms a large RBD-interface (~1275 $Å^2$, green surface in Figure 2D),
198 815 $Å^2$ of which is contributed by the heavy chain. Heavy-chain complementarity
199 determining regions form a cleft bordered on one side by two finger-like loops (CDRs
200 H1 and H2), opposite a thumb-like loop (extended CDR H3) between which the saddle
201 of the RBD (residues 470-492, Fig. 2C) is bound. CDRs L1 and L3 of the light chain

202 also contact the RBD, forming an additional cleft accommodating the side chain of
203 residue Y505, which projects from the surface of the RBD (Fig. 2C). The large surface
204 area buried at the interface is at the upper end of what is commonly observed for
205 antibody/antigen interactions [33,34]. This large interaction surface is reflective of the high
206 affinity of GAR05 (540 pM) and is also likely key to its broad neutralization potential,
207 despite its epitope covering a cluster of RBD residues commonly mutated in VOCs
208 (Fig. 2D, residues colored in yellow).
209
210 The binding mode of GAR05 is similar to that of mAb P2C-1F11, which has been
211 described as an ACE2 mimetic due to sharing extensive steric clash volume with ACE2
212 [35]. A primary difference, however, is the higher affinity and extremely long HCDR3
213 loop of GAR05, which wraps further than P2C-1F11around the RBD saddle targeted
214 by ACE2 (Supp. Fig. 7, top panels). A further class I targeting antibody, S2K146 [36],
215 has also been described as an ACE2 mimetic as it targets multiple evolutionarily
216 conserved residues utilised by ACE2, and displays broad resistance to VOCs. The
217 overall binding mode of S2K146 resembles that of GAR05, with the notable exception
218 that the orientation of the antibody heavy and light chains are reversed (approximately
219 180-degree rotation; Supp. Fig. 7, lower panels).
220
221 **Structural identification of a novel class 6 epitope**
222 We next performed structural studies on two broadly cross-reactive antibodies, GAR03
223 and GAR12, binding conserved epitopes in proximity to that of antibody S2H97 [12].
224 Initial cryo-EM studies using a GAR03-spike mix that had been incubated for 30 min
225 were unsuccessful due to significant aggregation and sample degradation. However, a
226 shorter 1 min incubation of GAR03:spike at a 3:1 ratio improved sample integrity and

227 this preparation was utilized to solve the structure of GAR03 bound to spike
228 glycoprotein (Supp. Fig. 6 and Supp. Table 2). Examination of the cryo-EM maps
229 revealed that density could not be observed for the N-terminal domain and RBD of one
230 of the three protomers (essentially an S1 domain), with the GAR03 Fab instead
231 occupying the space of the N-terminal domain while being bound to the RBD of an
232 adjacent protomer (Fig. 3A). Given that the S2 domain of all three protomers are
233 visible, we hypothesize that binding of GAR03 to an RBD causes the N-terminal
234 domain and RBD of an adjacent protomer to be displaced and become flexible, with
235 the averaging methods employed in single particle analysis cryo-EM making their
236 location unidentifiable. Subsequently, we crystalized GAR03 Fab in complex with the
237 RBD and solved the structure by X-ray crystallography to 2.75 Å resolution (Figure
238 3A, middle and right-hand panels), confirming the binding mode suggested by cryoEM,
239 whereby the bulk of the contact interface is mediated by the antibody light chain.
240 Competition binding assays suggested that GAR03 binds to an epitope shared with the
241 class 5 antibody S2H97 (Supp. Fig. 3). Surprisingly, however, mapping of the GAR03
242 structure onto the S2H97-RBD structure (PDB 7m7w) [12] revealed that, although
243 GAR03 and S2H97 block each other from binding to the RBD, the epitope overlap is
244 minimal (Fig. 3C and 3D – overlap colored green). More specifically, the GAR03
245 epitope occupies RBD surface extending from the class 5 epitope exemplified by
246 S2H97 to the class 3 epitope site, exemplified by the monoclonal antibody Sotrovimab)
247 (S309, PDB 7r6x[12], Fig. 3C – S2H97 in yellow and S309 in pink). This epitope is highly
248 conserved among sarbecoviruses, as highlighted by the cross-reactivity of GAR03 with
249 SARS-CoV-2, SARS-CoV-1, Pangolin CoV and Bat RaTG12-CoV RBD. BLI
250 competition experiments revealed that two other potently neutralizing antibodies,
251 GAR12 and GAR17, competed both with GAR03 and S309 (class 3 epitope) (Supp.

252 Fig. 8). However, the lack of competition with S2H97 suggests that GAR12 and
253 GAR17 presumably target regions more oriented towards the class 3 epitope site (Fig.
254 1C). To validate this hypothesis, we solve the crystal structure of GAR12 Fab in
255 complex with the RBD by X-ray crystallography to 2.25 Å resolution. Indeed, GAR12
256 binds to an epitope on the surface of the RBD that overlaps with S309 and abuts the
257 ACE2 contact surface (Fig. 3B-D, orange cartoon and surfaces). The GAR12 epitope
258 broadly avoids residues mutated in VOCs, thus demonstrating the broad and potent
259 neutralization of this antibody (Fig. 3B). We designate this epitope, spanning a
260 triangular surface between class 5, class 3 and class 1, as class 6 (Fig. 3C).
261
262 Superposition of GAR12, GAR03 and GAR05 antibodies to the trimeric spike protein
263 with the RBDs in the down position indicates that GAR12 is unimpeded and capable
264 of binding to spike in the fully down position (Fig. 3E – orange Fab cartoons). In
265 contrast, neither GAR03 (blue Fab cartoons) nor GAR05 (green Fab cartoons) can
266 access their respective RBD epitopes in the down position due to steric obstruction from
267 either neighboring N-terminal (both) or RBD domains (of adjacent protomers
268 (GAR05)) within the spike trimer (Fig. 3E).
269
270 **Live virus challenge in the K18-hACE2 mouse model**
271 To further validate monoclonal antibodies identified in this study, live virus challenge
272 experiments were carried out using the K18-hACE2 mouse model of SARS-CoV-2
273 infection in prophylaxis and therapeutic treatments [37,38]. For this purpose, we selected
274 three monoclonal antibodies with broad neutralization of variants of concern (Fig. 1C,
275 Fig. 1E, Supp. Fig. 5) and non-overlapping epitopes (Supp. Fig. 8), to enable future

276 application as combination therapy. More specifically, we selected GAR05 for class 1,
277 GAR12 for class 6 and GAR20 for class 4.
278
279 We initially evaluated the antibodies in a prophylaxis model using live SARS-CoV-2
280 virus (Wuhan). Mice were injected intraperitoneally with 30 mg/kg of monoclonal
281 antibody three days prior to challenge with 1 x 10^3 PFU live virus. Mice administered
282 with monoclonal antibodies maintained consistent body weight throughout the
283 challenge compared to mice administered with human IgG1 isotype control (Fig. 4A).
284 Moreover, treatment provided considerable protection from clinical symptoms, with
285 only control mice displaying severe scores (Fig. 4B). Viral titers in lung homogenates
286 from mice treated with monoclonal antibodies were significantly reduced compared to
287 isotype control and generally below the detection limit (Fig. 4C). Investigation of the
288 bronchoalveolar lavage fluids (BALF) revealed that all three treatment groups had
289 statistically significant reductions in inflammatory innate immune cells (macrophages
290 and neutrophils), while maintaining undetectable levels of lymphocytes (Supp. Fig. 9).
291 In a subsequent study, mice were challenged with Wuhan SARS-CoV-2 in a therapeutic
292 setting, with GAR05 administered post-viral challenge at 30 mg/kg. This experiment
293 revealed that, as had been observed in a prophylactic setting, mice treated with GAR05
294 were fully protected from viral challenge with no measurable weight loss (Fig. 4D),
295 reduction in clinical scores (Fig. 4E) or detectable lung viral titers (Fig. 4F). In a third
296 *in vivo* setting, GAR05 was used as a prophylactic modality (as above), and mice
297 challenged with the Delta (B.1.617.2) VOC. As had been observed for the initial live
298 virus challenge (Wuhan), mice treated with GAR05 were protected from the viral
299 challenge with the Delta VOC: indeed, no measurable reduction of either weight (Fig.

300 4G), clinical scores (Fig. 4H) could be observed, with undetectable viral titers in the
301 prophylaxis group (Fig. 4I).
302
303 Taken together, these findings demonstrate that the monoclonal antibodies developed
304 here, targeting non-overlapping epitopes, broadly and potently protect human ACE2
305 mice from SARS-CoV-2 live virus challenge, highlighting their potential for
306 therapeutic applications.
307
308 **Broad neutralization of Omicron VOCs**
309 The Omicron VOC and its subvariants have caused worldwide outbreaks, highlighting
310 the importance of broad antibody neutralization and mutational resistance [39,40]. When
311 Omicron BA.1 (B.1.1.529) first emerged in November 2021, we and others had shown
312 that only 1/6 monoclonal antibodies in clinical practice fully maintained activity,
313 namely the broadly neutralizing class 3 monoclonal Sotrovimab (S309) [10,41,42]. To
314 assess the potency of GAR05 and GAR12 against Omicron BA.1 and subvariants, we
315 performed *in vitro* neutralization assay using live virus. We observed that GAR05 and
316 GAR12 maintained their activity against the analyzed Omicron VOCs with IC_{50} values
317 ranging from 16.17 ng/ml to 337.6 ng/ml , with IC_{50}s considerably exceeding those of
318 Sotrovimab (S309)[41], particularly for the BA.2 subvariant which is not neutralized by
319 Sotrovimab (Fig. 5B).
320
321 **DISCUSSION**
322 The emergence of new SARS-CoV-2 VOCs, including Omicron variants, with
323 increased transmission and immune evasion, has triggered waves of infection
324 throughout the world [43]. Although existing vaccines remain protective against emerging

325 variants (albeit with reduced efficacy) [44], the vast majority of monoclonal antibodies do
326 not maintain activity against Omicron VOCs [10,45]. We show here that a sorting strategy
327 based on convalescent patient PBMCs, and RBDs bearing class-specific mutations, can
328 select for sarbecovirus cross-specific antibodies, including those binding to epitopes
329 outside the ACE2-binding site [14,46,47]. Such epitope-based sorting strategies using
330 mutant RBD may provide an efficient method to rapidly identify specific antibodies
331 against future variants of concern using variant RBDs or, alternately, those of ancestral
332 strains. This is exemplified by the work outlined here, based on convalescent patients
333 infected with the ancestral Wuhan strain, which allowed for the identification of
334 antibodies neutralizing a wide range of VOCs. In addition to broadly neutralizing
335 antibodies within each single epitope bin, our strategy allowed for the identification of
336 antibodies in multiple non-overlapping epitope bins, as highlighted by the identification
337 of three non-competing antibodies (GAR05, GAR12 and GAR20) that protect K18-
338 hACE2 mice from live SARS-CoV-2 challenge. This suggests possible future use for
339 combination therapy to increase efficacy and prevent mutational escape. Using cryo-
340 EM and crystallography, we define a new and highly conserved class 6 RBD epitope
341 on the surface of SARS-CoV-2 RBD, located between class 3 and class 5 epitopes.
342 While detailed mechanisms of action remain unknown, our data suggests that binding
343 of antibodies to this epitope may induce spike conformational rearrangements or
344 degradation, similarly to what has been observed for the antibody S2H97 [12]. Our results
345 also suggest that exposure to the original Wuhan SARS-CoV-2 RBD (through infection
346 or immunization) induces antibodies in patients that maintain potent and broad
347 neutralization potential against emerging VOCs. This is achieved by either targeting
348 the class 1/2 epitope in a manner resistant to VOCs (as illustrated by GAR05) or
349 alternatively by targeting rare and highly conserved epitopes, such as the novel class 6

350 epitope described here (as illustrated by GAR12), providing important guidance for
351 vaccine design. We conclude that epitope-based selection of SARS-CoV-2 neutralizing
352 antibodies from convalescent patients enables the identification of promising new
353 antibodies and epitopes against emerging variants of concern.
354
355
356 **ACKNOWLEDGEMENTS**

357 R.R. acknowledges funding from the Australian Research Council (ACR
358 DE190100985) and from the Garvan Institute of Medical Research (catalytic COVID
359 grant). D.C. acknowledges funding from the Medical Research Future Fund (MRFF
360 MRF2001739) and from the National Health and Medical Research Council (NHMRC
361 APP1157744 and APP1113904). A.G.S. acknowledges funding from the NHMRC
362 (APP1159347). R.A.B. acknowledges funding from the Snow Foundation. P.M.H.
363 acknowledges funding from the NHMRC (APP1175134), MRFF (MRF2007221),
364 NSW RNA Production Network, the Rainbow Foundation and UT. H.M.J.
365 acknowledges grants TRR130 from Deutsche Forschungsgemeinschaft (DFG), grants
366 01KI2043 and COVIM (NaFoUniMedCovid19; FKZ: 01KX2021) from the
367 Bundesministerium für Bildung und Forschung (BMBF), from the Kastner Foundation
368 and grants from the Bayerische Forschungsstiftung and the Bavarian Ministry of Art
369 and Science. Part of this work was performed on the MX2 beamline at the Australian
370 Synchrotron, part of ANSTO. The authors would like to thank the study participants
371 for their contribution to the research. They would like to acknowledge members of the
372 study group: Protocol Steering Committee – Andrew Lloyd (UNSW), John Kaldor
373 (UNSW), Greg Dore (UNSW), Tania Sorrell (Marie Bashir Institute), William
374 Rawlinson (NSWHP), Jeffrey Post (POWH), Bernard Hudson (RNSH), Dominic

375 Dwyer (NSWHP), Adam Bartlett (SCH), Sarah Sasson (UNSW) Nick Di Girolamo
376 (UNSW) and Daniel Lemberg (SCHN). Coordinating Centre - Marianne Byrne
377 (Clinical Trials Manager), Mohammed Hammoud (Post-Doctoral Fellow and Data
378 Manager), Andrew Lloyd (Investigator) and Roshana Sultan (Study co-ordinator). Site
379 Principal Investigators – Jeffrey Post (POWH), Michael Mina (Northern Beaches
380 Hospital), Bernard Hudson (RNSH), Nicky Gilroy (Westmead Hospital), Pam Konecny
381 (St George Hospital), Golo Ahlenstiel (Blacktown Mt Druitt Hospital), Adam Bartlett
382 (SCHN) and Gail Matthews (St Vincent's Hospital). Site co-ordinators – Dmitrii Shek
383 (Blacktown Mt Druitt Hospital); Katerina Mitsakos (RNSH); Renier Lagunday
384 (POWH); Sharon Robinson (St George Hospital); Lenae Terrill (Northern Beaches
385 Hospital); Neela Joshi, Ying Li and Satinder Gill (Westmead Hospital); Rebecca
386 Hickey and Alison Sevehon (St Vincent's Hospital). We also wish to thank and
387 acknowledge the use of the University of Wollongong Cryogenic Electron Microscopy
388 Facility at Molecular Horizons, the use of the Victor Chang Cardiac Research Institute
389 Innovation Centre, funded by the NSW Government, and the Electron Microscope Unit
390 at UNSW Sydney, funded in part by the NSW Government.
391

392 **AUTHOR CONTRIBUTIONS**

393 R.R., J.Y.H., R.A.B., D.C. and designed the project; J.Y.H. and H.B. performed human
394 B-cell sorting; R.R. generated SARS-CoV-2 proteins and amplified VH and VL from
395 single B-cells; M.S., S.H.J.B. and A.G.S. performed cryo-EM; D.B.L. performed X-
396 ray crystallography; M.D.J and P.M.H. performed animal experiments; G.W., S.G.T.
397 and W.D.R. performed neutralization experiments; R.R., J.Y.H., H. L., J.J., S.U., O.M.
398 and P.S. performed antibody production and BLI experiments; R.R., J.Y.H., D.B.L. and
399 D.C. wrote the manuscript with input from all other authors.

DECLARATION OF INTERESTS

The authors declare no competing financial interest.

404 **FIGURE LEGENDS**

405

406 **Figure 1: PBMC single cell sorting strategy and antibody characterization.** A:
407 Memory B cells were selected from convalescent patient PBMCs by gating on $CD3^-$
408 $CD19^+CD20^+CD10^-IgD^-IgG^+$ cells and single cells sorted by binding to fluorescently
409 labeled SARS-CoV-2 RBD or trimeric spike initially (left panel). In addition, using B:
410 mutant RBD protein (mutations colored in orange), single cells were sorted based on
411 FACS epitope bins. Red dots represent the B cells for which monoclonal antibodies
412 were amplified and characterized. C: Monoclonal antibodies analyzed, showing affinity
413 for SARS-CoV-2 RBD (Wuhan strain), neutralization potential and epitope class
414 (initial FACS epitope bin and validation). nn = non neutralizing. C: *In vitro*
415 neutralization of live SARS-CoV-2 virus (n=4).

416

417 **Figure 2: Structural characterization of the broadly neutralizing class 1 antibody**
418 **GAR05.** A: Cryo-EM structure of GAR05 Fab bound to trimeric spike showing full
419 antibody Fab occupancy of all the RBDs in the "up" conformation. B: Structure of
420 GAR05 bound to SARS-CoV-2 RBD based on the X-ray crystal structure, outlining the
421 antibody bound to the ACE2 "saddle" of the RBD. C: Interaction of the CDR regions
422 of the VH and VL domains with the RBD saddle and the Y505 side chain of the RBD.
423 D: Comparison of the ACE2 interface on the surface of RBD and the GAR05 epitope,
424 showing high overlap within the ACE2 saddle region. The large, buried surface area of
425 GAR05 (1275 $Å^2$) indeed blankets many key residues identified in VOCs, colored in
426 yellow, yet remarkably still binds all VOCs with potency.

427

428 **Figure 3: Structural identification of a novel class 6 epitope.** A: Cryo-EM structure
429 of spike trimer (three shades of grey surface) complexed with GAR03 (blue cartoon
430 and transparent surface) revealing a single GAR03 antibody Fab bound to trimeric spike
431 (left panel). Binding displaces the S1 domain (N-terminal domain and RBD) of one of
432 the protomers (disordered and not visible in the cryo-EM map), with the GAR03 Fab
433 binding to the RBD of the adjacent protomer. Middle and right panels show two
434 perspectives of the RBD-GAR03 crystal structure. The binding interface is dominated
435 by the GAR03 light chain (light blue cartoon; CDRs L1, L2 and L3) with more minor
436 contribution from the heavy chain (dark blue; CDR H3). The ACE2 interface of the
437 RBD (grey surface and cartoon) is shaded black, whilst omicron VOC mutation
438 positions are indicated by yellow sticks and surface B: Crystal structure of GAR12
439 (heavy and light chains colored dark and light orange) in complex with RBD (grey
440 cartoon and surface, with ACE2 interface colored black, and omicron VOCs colored
441 yellow). Two perspectives are shown. C: Global juxtaposition of GAR03 (blue
442 surfaces) and GAR12 (orange surfaces) with class 5 representative S2H97 (yellow) and
443 class 3 representative S309 (pink) shown against the RBD surface (grey, and black
444 indicating the RBD-ACE2 interface). D: RBD-interface comparisons. Left and middle
445 panels including GAR03 (blue) and S2H97 (yellow) and their overlap (green). The right
446 panel additionally includes the GAR12 (orange) and S309 interfaces (pink), and their
447 overlap (red). E. Spike trimer (three shades of grey surface) presented with all three
448 RBDs in the down conformation (PDB entry 6xm5) as viewed down the approximate
449 3-fold axis (left and middle panels); docked Fabs (middle panel) GAR03 (blue
450 cartoons), GAR05 (green cartoons), GAR12 (orange cartoons), as well as the primary
451 helix from ACE2 (yellow cartoon). Modelling indicates that only GAR12 is capable of

452 binding to spike with RBD in the down conformation (right panel, viewed from the
453 side).
454
455 **Figure 4: Protection of K18-hACE2 mice from live viral challenge.** Animals were
456 injected interperitoneally with 30 mg/kg of GAR05, GAR12, GAR20 or human IgG1
457 isotype control on d-3 prior to viral challenge for prophylactic studies (A-C,G-I) or d1
458 post challenge for therapeutic studies (D-F). Mice were challenged (d0) with $1x10^3$
459 PFU of intranasal Wuhan SARS-CoV-2 (A-C n=4, D-F n=6) or Delta VOC (B.1.167.2)
460 (G-I n=6) virus and monitored for 6 days, and euthanized (d6) for tissue collection.
461 Measurements of weight (percentage loss from initial weight, A/D/G), clinical score
462 (weight loss, eye closure, appearance of fur and posture, and respiration, B/E/H), and
463 viral titers (lung homogenates; plaque assay, C/F/I) shown.
464
465 **Figure 5: Neutralization of the Omicron VOCs.** A: SARS-CoV-2 neutralization (live
466 virus), Wuhan (A.2.2), Omicron VOCs BA1, BA2, BA5 (n=4). B: IC_{50} values (ng/ml)
467 reported for S309, GAR05 and GAR12 on Wuhan and Omicron VOCs. nn = non-
468 neutralizing.
469
470 **SUPPLEMENTARY FIGURE LEGENDS**
471 **Supplementary Figure 1: Overview of the PBMC sorting strategy.** Representative
472 flow cytometric plots of circulating IgD- CD27+ memory B cells in a convalescent
473 patient one month after SARS-CoV-2 infection. The cells were also stained with
474 fluorescent tetramers of SARS-CoV-2 RBD and SARS-CoV-2 spike protein for the
475 Sort 1 strategy. For the Sort 2 and Sort 3 strategies, cells were strained with WT RBD,
476 Mut1, Mut3 and SARS-CoV-1 RBD (replaced by Mut2 RBD in Sort 3).

477

478 **Supplementary Figure 2: Binding of monoclonal antibodies to SARS-CoV-2 RBD.**
479 A. Purified antibodies were initially screened by ELISA for their binding to RBD.
480 RBD was coated on a maxisorp ELISA plate at 2 µg/ml, incubated first with the purified
481 antibody at 100 µg/ml and then with HRP conjugated with anti-human IgG. B. Affinity
482 measurements by BLI. Streptavidin sensors were coated with biotinylated antibodies at
483 40 µg/ml, and association and dissociation constants measured using 2-fold serial
484 dilutions of the SARS-CoV-2 RBD from 400 to 50 nM. Raw binding curves are
485 represented in red and the fitted curves in black (K_D values in Figure 1C).

486

487 **Supplementary Figure 3: Epitope mapping through BLI competition.** Antibodies
488 were initially assessed for binding to the RBD (500 nM) pre-incubated with human
489 ACE2 Fc (1 µM) to identify class 1 and 2 antibodies. Additive binding signal indicates
490 co-binding while a decrease or absence of signal indicates competition. Non-class 1
491 and 2 antibodies were then evaluated for binding to RBD (500 nM) pre-incubated with
492 CR3022 IgG or with S2H97 IgG (1 µM) to identify the class 4 or 5 antibodies,
493 respectively. Finally, class 1/2 antibodies were evaluated for binding to the RBD
494 E484K mutant (500 nM) to suggest class 2 antibodies.

495

496 **Supplementary Figure 4: Cross reactivity to other sarbecovirus RBDs.** Monoclonal
497 antibodies were evaluated for binding to SARS-CoV-1, Bat RaTG13 and Pangolin CoV
498 by BLI. Biotinylated antibodies were captured onto streptavidin sensors and incubated
499 with the RBDs at 500 nM.

500

501 **Supplementary Figure 5: Neutralization of SARS-CoV-2 VOCs.** Antibodies were
502 evaluated for *in vitro* live SARS-CoV-2 virus neutralization in Vero E6 cells or
503 HEK293T cells expressing hACE2 (for the Delta variant only) (n=4).
504
505 **Supplementary Figure 6: Cryo-EM data processing flowchart.** Cryo-EM data
506 processing strategy along with the Fourier shell correction (FSC) curves on the final
507 maps.
508
509 **Supplementary Figure 7: S309 IgG, GAR03 and GAR12 BLI competition assay.**
510 A: To assess antibody epitopes, biotinylated antibodies were captured onto streptavidin
511 sensors and incubated with RBD (500 nM) pre-incubated with S309 IgG (1 μM) or
512 GAR03 IgG (1 μM). B: BLI assay demonstrating the non-overlapping binding of
513 GAR05, GAR12 and GAR20 on the surface of RBD. Biotinylated GAR12 was captured
514 onto streptavidin sensors and incubated with RBD, RBD pre-incubated with GAR05,
515 RBD pre-incubated with GAR20 or RBD pre-incubated with GAR05 and GAR20.
516 Increased binding curve shows that the antibodies do not compete.
517
518 **Supplementary Figure 8: BALF Differential cell counts from *in vivo* studies.**
519 Differential leukocyte (macrophages, neutrophils and lymphocytes) cell counts isolated
520 from bronchoalveolar lavage fluid (BALF) of Wuhan SARS-CoV-2 (A: prophylaxis,
521 and B: therapeutic model) or (C) Delta SARS-CoV-2 prophylactic model.
522
523

524
525 **METHODS**

526 **Antigen production and purification**

527 DNA encoding SARS-Cov-2 RBD (residues 319-541) was gene synthesized
528 (Genscript) and cloned into the pCEP4 mammalian expression vector (Invitrogen)
529 encoding a N-terminal IgG leader sequence and C-terminal Avi- and His-tag. RDB
530 mutants were generated by site-directed mutagenesis and splice-overlapping PCR.
531 Plasmids were transfected into Expi293 cells (Thermo Scientific) according to the
532 manufacturer's protocol and the protein expressed for 7 days at 37°C, 8% CO_2. Cell
533 cultures were clarified by centrifugation, dialyzed with PBS and the protein captured
534 with Talon resin (Thermo Scientific). The RBDs were eluted with 150 mM imidazole
535 in PBS, dialyzed with PBS and the purity assessed by visualization on SDS-PAGE. The
536 protein concentration was determined by measuring the Abs_{280nm}. For biotinylation of
537 the Avi-tag, the proteins were buffer exchanged into 20 mM HEPES pH 7.5 + 50 mM
538 NaCl using Zeba Spin desalting columns (Thermo Scientific). Then 10 mM ATP, 10
539 mM $MgCl_2$, 150 µM D-biotin and 3 µM BirA enzyme (purified in-house) in 50 mM
540 bicine buffer pH 8.3 was added to the protein and incubated for 1 h at 30°C. The
541 biotinylated protein was finally buffer exchanged back into PBS and the concentration
542 determined by measuring the Abs_{280nm}. The plasmid encoding the Wuhan SARS-CoV-
543 2 spike protein with C-terminal trimerization domain and His tag was kindly provided
544 by the Krammer lab (BEI Resources). The plasmid encoding the D614G VFLIP spike
545 protein with a C-terminal trimerization domain and Strept-tag was kindly provided by
546 the Saphire lab (La Jolla Institute of Immunology). The spike plasmids were transfected
547 into ExpiCHO and the protein expressed for 7 days at 32°C, 8% CO_2. After expression,
548 culture media were clarified by centrifugation and dialysed against 50 mM Tris pH 7.5
549 + 150 mM NaCl, and the Wuhan spike protein was purified using Talon Resin (Thermo

550 Scientific) while the D614G VFLIP spike was purified on a StrepTrap XT column (GE
551 Healthcare), according to the manufacturer's protocols. The spike proteins were further
552 purified on a Superose 6 gel filtration column (GE Healthcare) in 25 mM Tris pH 7.5
553 + 150 mM NaCl using an AKTA Pure FPLC instrument (GE Healthcare) to isolate the
554 trimeric protein (and remove S2 pre-fusion protein for the Wuhan spike). Finally, the
555 fractions containing the protein were concentrated using Amicon concentrators
556 (Merck), the protein concentration determined by measuring Abs_{280nm} and purity
557 assessed by visualization on SDS-PAGE gel. The spike protein was biotinylated using
558 EZ-Link NHS-PEG4-Biotin reagent (Thermo Scientific) as follows. Purified spike
559 protein was buffer exchanged into PBS using equilibrated Zeba Spin columns. The
560 protein concentration was determined and the spike biotinylated with EZ-Link NHS-
561 PEG4-Biotin at a 10:1 biotin-to-protein molar ratio for 30 min at room temperature.
562 Free biotin was removed from the spike by repeating the buffer exchange step in a
563 second Zeba Spin column equilibrated with 25 mM Tris pH 7.5 + 150 mM NaCl.
564
565 **Human B-cell sorting**
566 SARS-CoV-2 specific memory B cells were characterized and sorted via flow
567 cytometric tetramer assay essentially as previously described [2]: biotinylated SARS-
568 CoV-2 RBD (including mutant variants), spike and SARS-CoV-1 RBD were incubated
569 with Streptavidin-APC (BD), Streptavidin-PE (BD), Streptavidin-BB515 (BD) or
570 BV650-PE (BD) at a 4:1 molar ratio. Streptavidin conjugated fluorophores were titrated
571 onto biotinylated antigen in $1/10^{th}$ volume increments for 10 min per increment at 4°C.
572 Cryopreserved PBMCs from five convalescent patients were thawed and suspended in
573 pre-warmed RPMI-1640 media containing 10% FBS (sigma), 2 mM L-glutamine, 50
574 IU/ml penicillin and 50 µg/ml streptomycin. A maximum of $1x10^7$ cells were

575 resuspended in Fixable Viability Stain 700 (BD) diluted to 1:1000 in PBS and incubated
576 at 4°C for 20 min. Cells were washed twice with FACS buffer (PBS + 0.1% BSA) and
577 incubated with Human Fc block (5µl per $2x10^6$ cells; BD) at room temperature for 10
578 min. Cells were then washed twice with FACS buffer and resuspended in RBD or spike
579 tetramers at 1µg/ml (per tetramer) and incubated at 4°C for 30 min and washed twice
580 more with FACS buffer. Cells were finally suspended in a cell surface staining mix
581 containing (per test): 50 µl brilliant staining buffer (BD), 5 µl anti-human CD21
582 BV421, 5 µl anti-human IgD BV510, 5 µl anti-human CD19 BV711, 5 µl anti-human
583 CD20 APC-H7, 8 µl anti-human IgG BV786, 2 µl anti-human CD27 PE-CF594, 2 µl
584 anti-human CD38 PE-Cy7 and 0.5µl anti-human CD3 BB700 (all antibodies sourced
585 from BD). Surface staining incubation was performed at 4°C for 30 min, washed twice
586 and resuspended in FACS buffer for sorting. Immunophenotyping and index sorting
587 was performed on a BD FACSAria III where a minimum of 300,000 events were
588 acquired for each sample. Data analysis was performed using FlowJo version 10.7.1
589 (FlowJo LLC).
590
591 **Monoclonal antibody production and purification**
592 Sorted single B cells were collected into 96-well PCR plates containing 2 µL of Triton
593 X-100 (0.1%), dNTPs (5 nmol), oligo-dT primer (2.5 pmol) and RNAse inhibitor (1U
594 – Clontech). cDNA generation and amplification was performed following the
595 SmartSeq2 approach [26]. DNA encoding the antibody variable domains was amplified
596 by nested-PCR following the Tiller protocol [25]. DNA encoding VH and VL domains
597 were cloned into pCEP4 vectors encoding human IgG1 and light chains. After
598 validation by Sanger sequencing, plasmids were transfected into ExpiCHO (Thermo
599 Scientific) according to the manufacturer's protocol (1 µg DNA/ml of cells; 2:1 ratio

600 of heavy chain to light chain; following the maximum titer protocol). After 14 days,
601 cell culture media was clarified by centrifugation and the IgG captured using Protein G
602 resin (Genscript). The IgG were eluted from the Protein G resin using 100 mM glycine
603 pH 3.0, dialyzed with PBS and the purity assessed by visualization on SDS-PAGE. For
604 Fab production, the DNA encoding the VH domain was cloned into an in-house human
605 CH1 pCEP4 vectors with a C-terminus His tag. The production was performed in
606 ExpiCHO as for IgG. After 14 days, the cell culture media was clarified by
607 centrifugation, dialyzed against PBS and the Fab captured using Talon resin. The Fab
608 was eluted with 150 mM imidazole in PBS, dialyzed with PBS and the purity assessed
609 by visualization on SDS-PAGE. ACE2 fused to human IgG1 Fc domain was gene
610 synthesized (Genscript) and cloned into pCEP4. Expression was carried out in Expi293
611 cells for 7 days at 37°C, 8% CO_2. After expression, the ACE2 Fc fusion protein was
612 purified by Protein G resin as for human monoclonal antibody.
613
614 **Monoclonal antibody ELISA**
615 Maxisorp plates were coated with SARS-CoV-2 RBD at 2 µg/ml in carbonate coating
616 buffer overnight at 4ºC. The following day, plates were washed twice with PBS and
617 blocked in 4% milk in PBS-T (0.1% Tween 20) for 2 h. Plates were washed 3x with
618 PBS-T and incubated with the monoclonal antibodies diluted to 100 µg/ml in PBS for
619 1 h. Plates were then washed 3x with PBS-T and incubated with HRP-conjugated goat
620 Anti-human IgG/M antibody (Abcam) for 1h. Plates were finally washed 2x with PBS-
621 T and 1x with PBS and incubated with TMB substrate (Perkin Elmer) until the reaction
622 was quenched HCl. Plates were read at Abs 450nm (ClarioStar – BMG Labtech).
623

624 **Monoclonal antibody affinity measurements and competition assays by biolayer**
625 **interferometry (BLI)**
626 Purified monoclonal antibodies were buffer exchanged into PBS using equilibrated
627 Zeba Spin columns. The protein concentration was determined and the antibodies
628 biotinylated by incubating for 30 min at room temperature with EZ-Link NHS-PEG4-
629 Biotinylation reagent (Thermo Scientific) at a 10:1 biotin-to-protein ratio. Free biotin
630 was removed by repeating the buffer exchange step in a second Zeba Spin column
631 equilibrated with PBS. Affinity of interactions between biotinylated antibodies and
632 purified soluble RBD proteins were measured by Biolayer Interferometry (BLItz,
633 ForteBio). Streptavidin biosensors were rehydrated in PBS containing 0.1% BSA for 1
634 h at room temperature. Biotinylated antibody was loaded onto the sensors "on-line"
635 using an advanced kinetics protocol, and global fits were obtained for the binding
636 kinetics by running associations and dissociations of RBD proteins at a suitable range
637 of molar concentrations (2-fold serial dilution ranging from 800 nM to 50 nM). The
638 global dissociation constant (K_D) for each 1:1 binding interaction was determined using
639 the BlitzPro 1.2.1.3 software. For competition assays, RBD at 400 nM was pre-
640 incubated with competitor (ACE2 Fc or unconjugated antibody) at 1 μM for 10 min at
641 room temperature.
642
643 **SARS-CoV2 neutralization assay**
644 Serial 2-fold dilutions of test monoclonal antibody were prepared, and neutralization
645 assay was performed in Vero E6 cells (HEK293T cells over-expressing the human
646 ACE2 receptor for the Delta VOC), as previously described [48].
647
648 **X-ray crystallography**

649 Antibody Fab fragments were purified further via size-exclusion chromatography using
650 an S200 increase 10/30 column (GE Healthcare) equilibrated with 25 mM Tris (pH
651 8.0), 200 mM NaCl. C-terminally His-tagged SARS-CoV-2 RBD (residues 333-528)
652 was expressed and purified as for the other RBDs. Fab and RBD were
653 stoichiometrically combined and concentrated to approximately 5 mg/ml. Solutions
654 were combined with an equal volume (2 μL) of well solution in a vapor diffusion
655 hanging drop crystallization format. For the RBD-GAR05 complex, the well solution
656 comprised 100 mM citrate pH 4.25, 500 mM LiCl and 13% (w/v) PEG 6000. For the
657 RBD-GAR12 complex, the well solution comprised 100 mM of the MMT buffer
658 system (pH 6.6) (Molecular Dimensions; comprising malic acid, 2-ethanesulfonic acid
659 and trisaminomethane), and 19% (w/v) PEG6K. To facilitate crystallization this
660 complex also included an additional antibody Fab (10G4) which binds to a different
661 epitope of the RBD (to be described elsewhere; Mazigi et al). For the RDB-GAR12
662 complex the well solution comprised 100 mM ammonium citrate (pH 5.5), 20% (w/v)
663 PEG3350. Crystals were flash frozen in liquid nitrogen with no cryoprotection regime.
664 Diffraction data were collected at the Australian Synchrotron on beamline MX2 using
665 a Dectris Eiger X16M detector. For all crystals a 360° sweep of data were deconvoluted
666 into 3600 x 0.1° oscillation images which were indexed and integrated by XDS [49].
667 Space groups were determined with Pointless [50] and scaling and merging performed
668 with Aimless [51], both components of CCP4 [52]. Structures were determined by
669 molecular replacement using Phaser [53], using generic human Fab fragments (containing
670 kappa light chain for Fabs GAR05, GAR12 and 10G4, and containing a lambda light
671 chain for GAR03) and SARS-CoV-2 RBD as search models. All structures contained
672 one complex (1:1, or 1:1:1 for GAR03) in the asymmetric unit. Structure refinement
673 was performed using Refmac [54] then phenix.refine [55] between rounds of manual

674 inspection and model adjustment using Coot [56]. The electron density for many parts of
675 the GAR05 model, in particular, was poorly defined, commensurate with the low
676 resolution and very high B-factors, hence refinement employed a combination of
677 reference model and secondary structure restraints, however some of the best density
678 exists at the interface between the antibody and the RBD, providing confidence in the
679 Fab-RBD juxtaposition. Model validation was performed using the Molprobity server
680 [57]. Diffraction data and model refinement statistics are shown in Supplementary Table
681 1.
682
683 **Cryo-electron microscopy**
684 For sample preparation, D614G VFLIP spike trimer and Fab (molar ratio of 1:3) was
685 incubated at room temperature for either 30 min (GAR05 or 1 min (GAR03) before
686 application to holey gold grids and freezing. 3.5 µl of each sample was applied to
687 1.2/1.3 UltrAuFoil grids (Quantifoil) which had been glow-discharged for 1 min at 15
688 mA in an EasiGlow (Pelco). Plunge freezing was performed using a Vitrobot Mark IV
689 (Thermo Scientific) with 0 blot force, 4 s blot time and 100% humidity at 22 °C. Grids
690 were initially screened on a Talos Arctica Electron Microscope (Thermo Scientific) and
691 assessed for particle concentration, integrity, and ice thickness. For final data
692 collection, grids were transferred to a Titan Krios Electron Microscope (Thermo
693 Scientific) operating at 300 kV equipped with a BioQuantum K2 (Gatan) with the slit
694 set to 20 ev. Movies were recorded using EPU with a calibrated pixel size of 1.08 Å, a
695 total dose of 50 electrons spread over 50 frames and a total exposure time of 5 s. All
696 processing was performed in cryoSPARC [58]. Initial particles were picked using the
697 "blob" protocol, and these 2D classified to create templates to pick the datasets.
698 Extracted particles were subjected to multiple rounds of 2D classification, *ab initio*

699 reconstruction and heterogenous refinement to sort the particles into discrete structures
700 (Supp. Fig. 6). In the case of the D614G VFLIP spike trimer bound to GAR03, focussed
701 refinement was utilised on the region corresponding to GAR03:RBD in order to
702 increase the detail in this area (Supp. Fig. 6). An atomic model for GAR03 Fv was
703 generated using ABodyBuilder [59], the constant domains CH1 and lambda CL added
704 using PDB ID 7m3i [60], and fitted into the focussed map. This model was combined with
705 an atomic model for the entire spike complex (PDB ID 6xlu [61]), introducing the D614G
706 VFLIP mutations and removing regions with little to no density. This model was then
707 used to create a combined map (with the focussed and unfocussed maps) in Phenix [62]
708 and the model was fitted/refined using Coot [56], ISOLDE [63] and Phenix. Supp. Fig. 6
709 provides a summary of the data collection and refinement statistics.
710
711 **Animal experiments**
712 All mouse experiments were performed according to ethical guidelines as set out by the
713 Sydney Local Health District (SLHD) Animal Ethics and Welfare Committee, which
714 adhere to the Australian Code for the Care and Use of Animals for Scientific Purposes
715 (2013) as set out by the National Health and Medical Research Council of Australia.
716 SARS-CoV-2 mouse infection experiments were approved by the SLHD Institutional
717 Biosafety Committee. For Wuhan SARS-CoV-2 prophylaxis assays, 4 female
718 hemizygous K18-hACE2 mice (B6.Cg-Tg(K18-hACE2)2Prlmn/J, stock Nb. 034860,
719 Jackson Lab) were injected on day -3 (prior to intranasal viral challenge with 1 x
720 10^3 PFU of Wuhan SARS-CoV-2 (Isolate AUS/VIC01/2020)) intraperitoneally with
721 30mg/kg for each individual antibody (GAR05, GAR12, GAR20 and a human IgG1
722 isotype control (Bio X Cell) at 3mg/ml in PBS) in a 200 µl volume. For Wuhan SARS-
723 CoV-2 therapeutic assays, 6 female hemizygous K18-hACE2 mice (B6.Cg-Tg(K18-

724 hACE2)2Prlmn/J, stock Nb. 034860, Jackson Lab) were injected on day 1 (post
725 intranasal viral challenge with 1 x 10^3 PFU of Wuhan SARS-CoV-2 (Isolate
726 AUS/VIC01/2020)) intraperitoneally with 30mg/kg GAR05 or a human IgG1 isotype
727 control (Bio X Cell) at 3mg/ml in PBS) in a 200 µl volume. For Delta SARS-CoV-2
728 prophylaxis assays, 6 female hemizygous K18-hACE2 mice (B6.Cg-Tg(K18-
729 hACE2)2Prlmn/J, stock Nb. 034860, Jackson Lab) were injected on day -3 (prior to
730 intranasal viral challenge with 1 x 10^3 PFU of Delta SARS-CoV-2 (B1.617.2))
731 intraperitoneally with 30mg/kg GAR05 and a human IgG1 isotype control (Bio X Cell)
732 at 3mg/ml in PBS) in a 200 µl volume. On day 0, treated mice were moved to the
733 PC3/BSL3 lab and intranasally inoculated with 1 x 10^3 PFU of Wuhan SARS-CoV-2
734 (Isolate AUS/VIC01/2020) or Delta SARS-CoV-2 (B1.617.2) in a 30 µl volume as
735 previously described [38]. Mice were weighed, monitored and scored for clinical
736 symptoms (weight loss, eye closure, appearance of fur and posture, and respiration)
737 daily and any mice that reached the ethical endpoints were humanely euthanised. On
738 day 6, all mice were humanely euthanised. Multi-lobe lungs were tied off and BALF
739 was collected from the single lobe via lung lavage with 1 mL HANKS solution using a
740 blunted 19-gauge needle inserted into the trachea. BALF was centrifuged (300 *g*, 4 °C,
741 7 min), and supernatants collected and snap frozen. Cell pellets were treated with
742 200 µL Red Blood Cell Lysis Buffer (Thermo Scientific) for 5 min, followed by
743 addition of 700 µL HANKS solution to inactivate the reaction and then centrifuged
744 again. Cell pellets were resuspended in 160 µL HANKS solution and enumerated using
745 a haemocytometer (Sigma-Aldrich). Differential cell BALF counts were performed by
746 loading 70 µl of the BALF cell pellet into a cytospin funnel and centrifuging (300×*g*,
747 7 min) and were left to airdry overnight. Following drying, slides were stained using
748 the Quick Dip stain kit (POCD Scientific) as per manufacturer's instructions. Multi-

749 lobe lungs were collected and snap frozen on dry ice. Lung homogenates were prepared
750 fresh, with the third multi-lobe lungs placed into a gentleMACS C-tube (Miltenyi
751 Biotec) containing 2 mL HANKS solution. Tissue was homogenised using a
752 gentleMACS tissue homogeniser, after which homogenates were centrifuged (300×*g*,
753 7 min) to pellet cells, followed by collection of supernatants for plaque assays. The
754 significance of differences between experimental groups was evaluated by one-way
755 analysis of variance (ANOVA), with pairwise comparison of multi-grouped data sets
756 achieved using Tukey's or Dunnett's *post-hoc* test. Differences were considered
757 statistically significant when $p \leq 0.05$.
758
759 **Supplementary Table 1: Diffraction data and model refinement statistics.** Values
760 in parentheses represent values for the highest resolution shell.
761
762 **Supplementary Table 2: Cryo-EM data collection and refinement.**
763
764
765
766
767

768 **REFERENCES**

769 1 World Health Organization Coronavirus (COVID-19) Dashboard.
770 2 Abayasingam, A. *et al.* Long-term persistence of RBD(+) memory B cells
771 encoding neutralizing antibodies in SARS-CoV-2 infection. *Cell Rep Med* **2**, 100228,
772 doi:10.1016/j.xcrm.2021.100228 (2021).
773 3 Seow, J. *et al.* Longitudinal observation and decline of neutralizing antibody
774 responses in the three months following SARS-CoV-2 infection in humans. *Nat*
775 *Microbiol* **5**, 1598-1607, doi:10.1038/s41564-020-00813-8 (2020).
776 4 Noy-Porat, T. *et al.* A panel of human neutralizing mAbs targeting SARS-
777 CoV-2 spike at multiple epitopes. *Nat Commun* **11**, 4303, doi:10.1038/s41467-020-
778 18159-4 (2020).
779 5 Piccoli, L. *et al.* Mapping Neutralizing and Immunodominant Sites on the
780 SARS-CoV-2 Spike Receptor-Binding Domain by Structure-Guided High-Resolution
781 Serology. *Cell* **183**, 1024-1042 e1021, doi:10.1016/j.cell.2020.09.037 (2020).
782 6 Barnes, C. O. *et al.* SARS-CoV-2 neutralizing antibody structures inform
783 therapeutic strategies. *Nature* **588**, 682-687, doi:10.1038/s41586-020-2852-1 (2020).
784 7 Greaney, A. J. *et al.* Antibodies elicited by mRNA-1273 vaccination bind
785 more broadly to the receptor binding domain than do those from SARS-CoV-2
786 infection. *Sci Transl Med* **13**, doi:10.1126/scitranslmed.abi9915 (2021).
787 8 Wang, P. *et al.* Increased resistance of SARS-CoV-2 variant P.1 to antibody
788 neutralization. *Cell Host Microbe* **29**, 747-751 e744, doi:10.1016/j.chom.2021.04.007
789 (2021).
790 9 Wang, P. *et al.* Antibody resistance of SARS-CoV-2 variants B.1.351 and
791 B.1.1.7. *Nature* **593**, 130-135, doi:10.1038/s41586-021-03398-2 (2021).
792 10 Aggarwal, A. *et al.* SARS-CoV-2 Omicron: evasion of potent humoral
793 responses and resistance to clinical immunotherapeutics relative to viral variants of
794 concern. *medRxiv*, 2021.2012.2014.21267772, doi:10.1101/2021.12.14.21267772
795 (2021).
796 11 Robbiani, D. F. *et al.* Convergent antibody responses to SARS-CoV-2 in
797 convalescent individuals. *Nature* **584**, 437-442, doi:10.1038/s41586-020-2456-9
798 (2020).
799 12 Starr, T. N. *et al.* SARS-CoV-2 RBD antibodies that maximize breadth and
800 resistance to escape. *Nature* **597**, 97-102, doi:10.1038/s41586-021-03807-6 (2021).
801 13 Onodera, T. *et al.* A SARS-CoV-2 Antibody Broadly Neutralizes SARS-
802 related Coronaviruses and Variants by Coordinated Recognition of a Virus
803 Vulnerable Site. *Immunity*, doi:10.1016/j.immuni.2021.08.025 (2021).
804 14 Burnett, D. L. *et al.* Immunizations with diverse sarbecovirus receptor-binding
805 domains elicit SARS-CoV-2 neutralizing antibodies against a conserved site of
806 vulnerability. *Immunity*, doi:10.1016/j.immuni.2021.10.019 (2021).
807 15 Rappazzo, C. G. *et al.* Broad and potent activity against SARS-like viruses by
808 an engineered human monoclonal antibody. *Science* **371**, 823-829,
809 doi:10.1126/science.abf4830 (2021).
810 16 Cohen, M. S. *et al.* Effect of Bamlanivimab vs Placebo on Incidence of
811 COVID-19 Among Residents and Staff of Skilled Nursing and Assisted Living
812 Facilities: A Randomized Clinical Trial. *JAMA* **326**, 46-55,
813 doi:10.1001/jama.2021.8828 (2021).
814 17 Chen, P. *et al.* SARS-CoV-2 Neutralizing Antibody LY-CoV555 in
815 Outpatients with Covid-19. *N Engl J Med*, doi:10.1056/NEJMoa2029849 (2020).

816 18 Group, R. C. *et al.* Casirivimab and imdevimab in patients admitted to hospital
817 with COVID-19 (RECOVERY): a randomised, controlled, open-label, platform trial.
818 *medRxiv*, 2021.2006.2015.21258542, doi:10.1101/2021.06.15.21258542 (2021).
819 19 Pinto, D. *et al.* Cross-neutralization of SARS-CoV-2 by a human monoclonal
820 SARS-CoV antibody. *Nature* **583**, 290-295, doi:10.1038/s41586-020-2349-y (2020).
821 20 Ku, Z. *et al.* Molecular determinants and mechanism for antibody cocktail
822 preventing SARS-CoV-2 escape. *Nat Commun* **12**, 469, doi:10.1038/s41467-020-
823 20789-7 (2021).
824 21 Sun, Y. *et al.* Structure-based development of three- and four-antibody
825 cocktails against SARS-CoV-2 via multiple mechanisms. *Cell Res* **31**, 597-600,
826 doi:10.1038/s41422-021-00497-7 (2021).
827 22 COSIN.study. https://kirby.unsw.edu.au/project/natural-history-cohort-
828 following-sars-cov-2-infection. (2020).
829 23 Amanat, F. *et al.* A serological assay to detect SARS-CoV-2 seroconversion in
830 humans. *Nat Med* **26**, 1033-1036, doi:10.1038/s41591-020-0913-5 (2020).
831 24 Rouet, R. *et al.* Potent SARS-CoV-2 binding and neutralization through
832 maturation of iconic SARS-CoV-1 antibodies. *MAbs* **13**, 1922134,
833 doi:10.1080/19420862.2021.1922134 (2021).
834 25 Tiller, T. *et al.* Efficient generation of monoclonal antibodies from single
835 human B cells by single cell RT-PCR and expression vector cloning. *J Immunol*
836 *Methods* **329**, 112-124, doi:10.1016/j.jim.2007.09.017 (2008).
837 26 Picelli, S. *et al.* Full-length RNA-seq from single cells using Smart-seq2. *Nat*
838 *Protoc* **9**, 171-181, doi:10.1038/nprot.2014.006 (2014).
839 27 Yuan, M. *et al.* Structural basis of a shared antibody response to SARS-CoV-
840 2. *Science* **369**, 1119-1123, doi:10.1126/science.abd2321 (2020).
841 28 Tian, X. *et al.* Potent binding of 2019 novel coronavirus spike protein by a
842 SARS coronavirus-specific human monoclonal antibody. *Emerg Microbes Infect* **9**,
843 382-385, doi:10.1080/22221751.2020.1729069 (2020).
844 29 Yuan, M. *et al.* A highly conserved cryptic epitope in the receptor binding
845 domains of SARS-CoV-2 and SARS-CoV. *Science* **368**, 630-633,
846 doi:10.1126/science.abb7269 (2020).
847 30 Jette, C. A. *et al.* Broad cross-reactivity across sarbecoviruses exhibited by a
848 subset of COVID-19 donor-derived neutralizing antibodies. *Cell Rep* **37**, 110188,
849 doi:10.1016/j.celrep.2021.110188 (2021).
850 31 Olmedillas, E. *et al.* Structure-based design of a highly stable, covalently-
851 linked SARS-CoV-2 spike trimer with improved structural properties and
852 immunogenicity. *bioRxiv*, 2021.2005.2006.441046, doi:10.1101/2021.05.06.441046
853 (2021).
854 32 Barnes, C. O. *et al.* Structures of Human Antibodies Bound to SARS-CoV-2
855 Spike Reveal Common Epitopes and Recurrent Features of Antibodies. *Cell* **182**, 828-
856 842 e816, doi:10.1016/j.cell.2020.06.025 (2020).
857 33 Davies, D. R. & Cohen, G. H. Interactions of protein antigens with antibodies.
858 *Proc Natl Acad Sci U S A* **93**, 7-12 (1996).
859 34 Ramaraj, T., Angel, T., Dratz, E. A., Jesaitis, A. J. & Mumey, B. Antigen-
860 antibody interface properties: composition, residue interactions, and features of 53
861 non-redundant structures. *Biochim Biophys Acta* **1824**, 520-532,
862 doi:10.1016/j.bbapap.2011.12.007 (2012).
863 35 Ge, J. *et al.* Antibody neutralization of SARS-CoV-2 through ACE2 receptor
864 mimicry. *Nat Commun* **12**, 250, doi:10.1038/s41467-020-20501-9 (2021).

36 Park, Y. J. *et al.* Antibody-mediated broad sarbecovirus neutralization through ACE2 molecular mimicry. *Science* **375**, 449-454, doi:10.1126/science.abm8143 (2022).
37 Johansen, M. D. *et al.* Animal and translational models of SARS-CoV-2 infection and COVID-19. *Mucosal Immunol* **13**, 877-891, doi:10.1038/s41385-020-00340-z (2020).
38 Counoupas, C. *et al.* A single dose, BCG-adjuvanted COVID-19 vaccine provides sterilising immunity against SARS-CoV-2 infection. *NPJ Vaccines* **6**, 143, doi:10.1038/s41541-021-00406-4 (2021).
39 Dyer, O. Covid-19: South Africa's surge in cases deepens alarm over omicron variant. *BMJ* **375**, n3013, doi:10.1136/bmj.n3013 (2021).
40 Pulliam, J. R. C. *et al.* Increased risk of SARS-CoV-2 reinfection associated with emergence of the Omicron variant in South Africa. *medRxiv*, 2021.2011.2011.21266068, doi:10.1101/2021.11.11.21266068 (2021).
41 Touret, F., Baronti, C., Bouzidi, H. S. & de Lamballerie, X. In vitro evaluation of therapeutic antibodies against a SARS-CoV-2 Omicron B.1.1.529 isolate. *bioRxiv*, 2022.2001.2001.474639, doi:10.1101/2022.01.01.474639 (2022).
42 Cameroni, E. *et al.* Broadly neutralizing antibodies overcome SARS-CoV-2 Omicron antigenic shift. *bioRxiv*, doi:10.1101/2021.12.12.472269 (2021).
43 Tao, K. *et al.* The biological and clinical significance of emerging SARS-CoV-2 variants. *Nat Rev Genet*, doi:10.1038/s41576-021-00408-x (2021).
44 Lopez Bernal, J. *et al.* Effectiveness of Covid-19 Vaccines against the B.1.617.2 (Delta) Variant. *N Engl J Med* **385**, 585-594, doi:10.1056/NEJMoa2108891 (2021).
45 Falcone, M. *et al.* Efficacy of Bamlanivimab/Etesevimab and Casirivimab/Imdevimab in Preventing Progression to Severe COVID-19 and Role of Variants of Concern. *Infect Dis Ther* **10**, 2479-2488, doi:10.1007/s40121-021-00525-4 (2021).
46 Feldman, J. *et al.* Naive human B cells engage the receptor binding domain of SARS-CoV-2, variants of concern, and related sarbecoviruses. *Sci Immunol* **6**, eabl5842, doi:10.1126/sciimmunol.abl5842 (2021).
47 Shinnakasu, R. *et al.* Glycan engineering of the SARS-CoV-2 receptor-binding domain elicits cross-neutralizing antibodies for SARS-related viruses. *J Exp Med* **218**, doi:10.1084/jem.20211003 (2021).
48 Tea, F. *et al.* SARS-CoV-2 neutralizing antibodies: Longevity, breadth, and evasion by emerging viral variants. *PLoS Med* **18**, e1003656, doi:10.1371/journal.pmed.1003656 (2021).
49 Kabsch, W. Xds. *Acta Crystallogr D Biol Crystallogr* **66**, 125-132, doi:10.1107/S0907444909047337 (2010).
50 Evans, P. R. An introduction to data reduction: space-group determination, scaling and intensity statistics. *Acta Crystallogr D Biol Crystallogr* **67**, 282-292, doi:10.1107/S090744491003982X (2011).
51 Evans, P. R. & Murshudov, G. N. How good are my data and what is the resolution? *Acta Crystallographica Section D* **69**, 1204-1214, doi:doi:10.1107/S0907444913000061 (2013).
52 Winn, M. D. *et al.* Overview of the CCP4 suite and current developments. *Acta Crystallogr D Biol Crystallogr* **67**, 235-242, doi:10.1107/S0907444910045749 (2011).

53 McCoy, A. J. Solving structures of protein complexes by molecular replacement with Phaser. *Acta Crystallogr D Biol Crystallogr* **63**, 32-41, doi:10.1107/S0907444906045975 (2007).
54 Murshudov, G. N. *et al.* REFMAC5 for the refinement of macromolecular crystal structures. *Acta Crystallogr D Biol Crystallogr* **67**, 355-367, doi:10.1107/S0907444911001314 (2011).
55 Afonine, P. V. *et al.* Towards automated crystallographic structure refinement with phenix.refine. *Acta Crystallogr D Biol Crystallogr* **68**, 352-367, doi:10.1107/S0907444912001308 (2012).
56 Emsley, P., Lohkamp, B., Scott, W. G. & Cowtan, K. Features and development of Coot. *Acta Crystallogr D Biol Crystallogr* **66**, 486-501, doi:10.1107/S0907444910007493 (2010).
57 Chen, V. B. *et al.* MolProbity: all-atom structure validation for macromolecular crystallography. *Acta Crystallogr D Biol Crystallogr* **66**, 12-21, doi:S0907444909042073 [pii]
10.1107/S0907444909042073 (2010).
58 Punjani, A., Rubinstein, J. L., Fleet, D. J. & Brubaker, M. A. cryoSPARC: algorithms for rapid unsupervised cryo-EM structure determination. *Nat Methods* **14**, 290-296, doi:10.1038/nmeth.4169 (2017).
59 Leem, J., Dunbar, J., Georges, G., Shi, J. & Deane, C. M. ABodyBuilder: Automated antibody structure prediction with data-driven accuracy estimation. *MAbs* **8**, 1259-1268, doi:10.1080/19420862.2016.1205773 (2016).
60 Jennewein, M. F. *et al.* Isolation and characterization of cross-neutralizing coronavirus antibodies from COVID-19+ subjects. *Cell Rep* **36**, 109353, doi:10.1016/j.celrep.2021.109353 (2021).
61 Zhou, T. *et al.* Cryo-EM Structures Delineate a pH-Dependent Switch that Mediates Endosomal Positioning of SARS-CoV-2 Spike Receptor-Binding Domains. *bioRxiv*, doi:10.1101/2020.07.04.187989 (2020).
62 Liebschner, D. *et al.* Macromolecular structure determination using X-rays, neutrons and electrons: recent developments in Phenix. *Acta Crystallogr D Struct Biol* **75**, 861-877, doi:10.1107/S2059798319011471 (2019).
63 Croll, T. I. ISOLDE: a physically realistic environment for model building into low-resolution electron-density maps. *Acta Crystallogr D Struct Biol* **74**, 519-530, doi:10.1107/S2059798318002425 (2018).

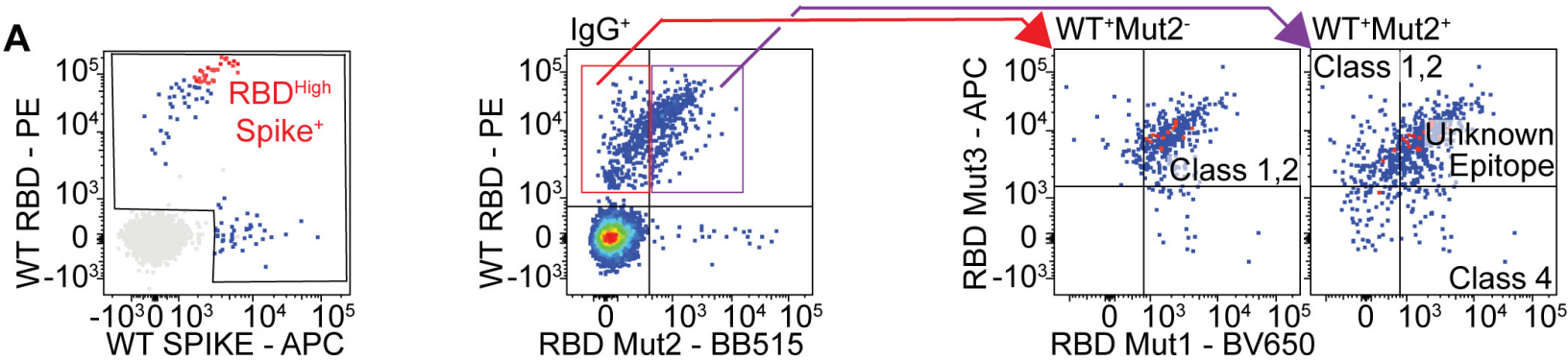

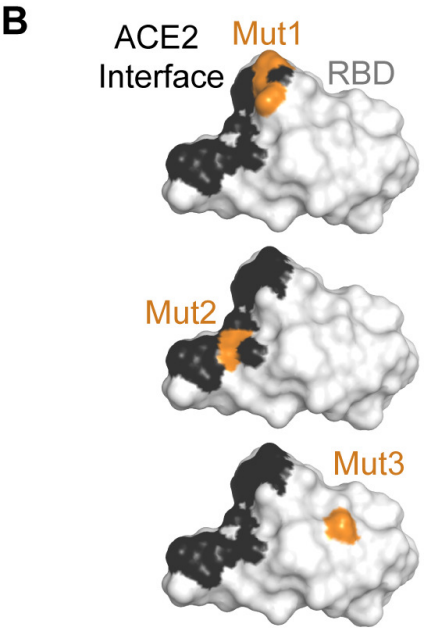

C

Antibody name	Affinity/RBD (nM)	Wuhan IC_{50} (ng/ml)	Delta IC_{50} (ng/ml)	FACS epitope bin	Validated class
GAR01	292	nn	nn	RBD	5,6
GAR03	0.31	>20000	nn	RBD	6
GAR04	23.3	12	nn	RBD	2
GAR05	0.54	28	50	RBD	1
GAR06	37.8	455	8042	RBD	1
GAR07	2.87	287	582	unknown	1
GAR09	1.47	106	113	1,2	1
GAR11	20.6	10000	nn	4	4
GAR12	0.20	182	255	1,2	6
GAR13	0.30	nn	nn	1,2	4
GAR14	2.15	nn	nn	1,2	4
GAR15	1.30	157	74	unknown	1
GAR16	3.28	nn	nn	4,5	4
GAR17	1.95	162	nn	unknown	3,6
GAR18	0.24	14630	nn	unknown	6
GAR20	0.60	5470	3770	4	4

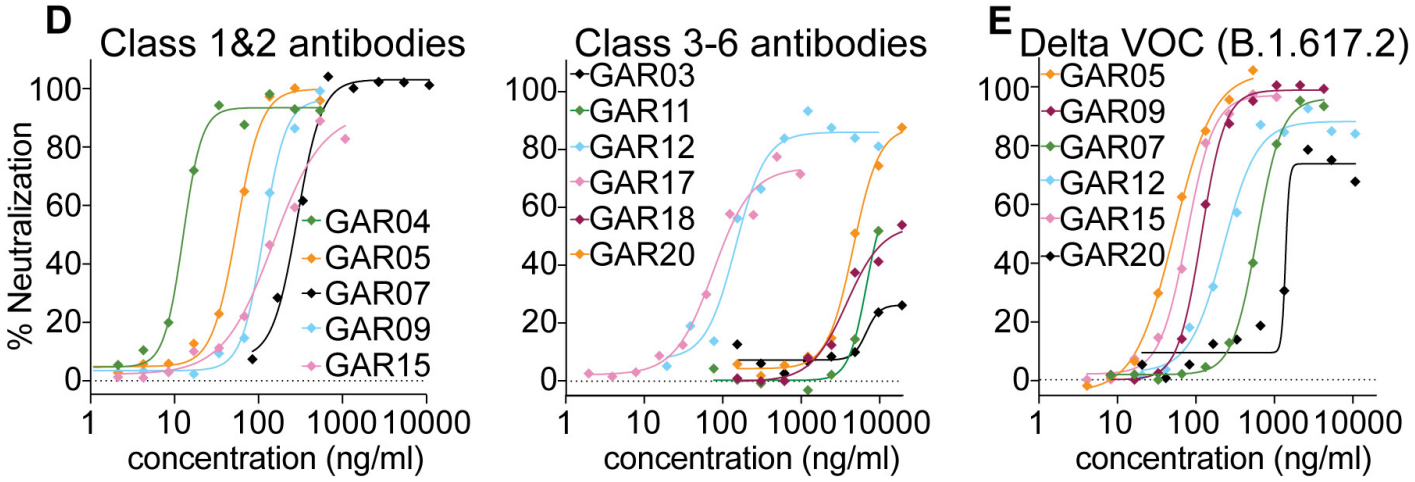

Figure 1

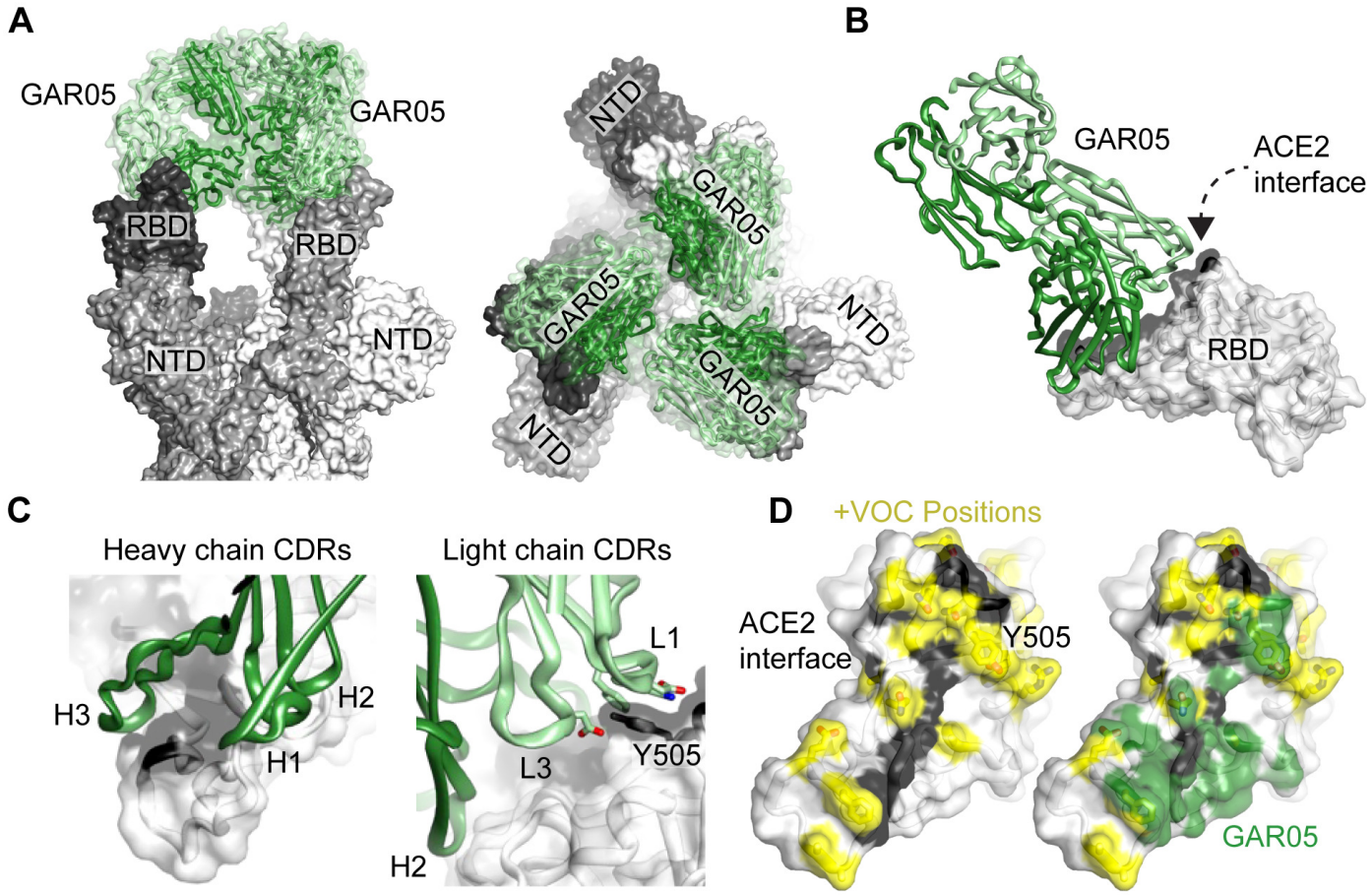
A
GAR05
GAR05
RBD
RBD
NTD
NTD
NTD
GAR05
GAR05
GAR05
NTD
NTD
B
GAR05
ACE2
interface
RBD
C
Heavy chain CDRs
H3
H2
H1
Light chain CDRs
L1
L3
Y505
H2
D
+VOC Positions
ACE2
interface
Y505
GAR05

Figure 2

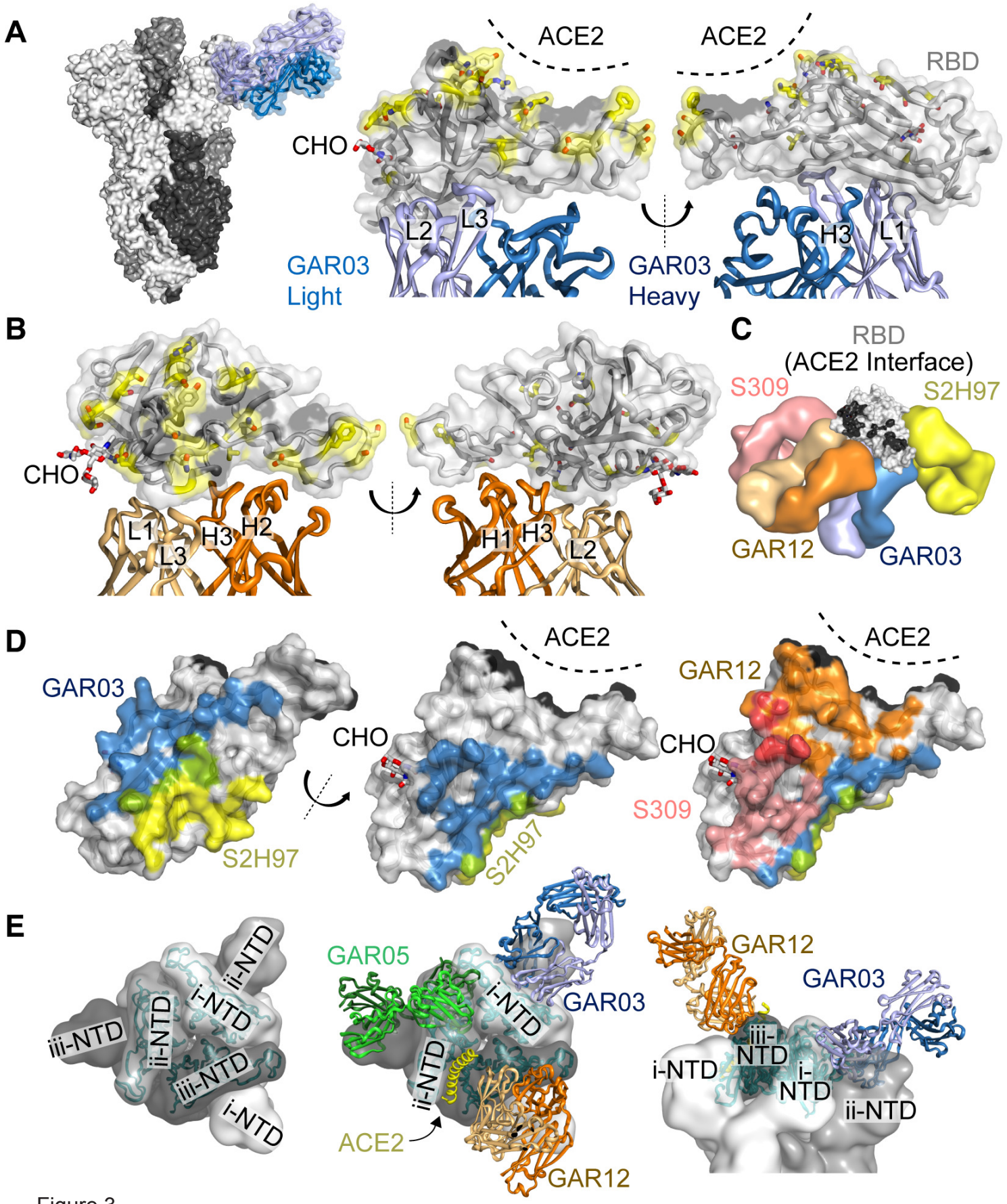
A
ACE2
ACE2
RBD
CHO
L2
L3
H3
L1
GAR03
Light
GAR03
Heavy
B
CHO
L1
L3
H3
H2
H1
H3
L2
C
RBD
(ACE2 Interface)
S309
S2H97
GAR12
GAR03
D
GAR03
S2H97
CHO
ACE2
S2H97
GAR12
CHO
ACE2
S309
E
ii-NTD
i-NTD
iii-NTD
ii-NTD
iii-NTD
i-NTD
GAR05
i-NTD
GAR03
ii-NTD
ACE2
GAR12
GAR12
GAR03
iii-NTD
i-NTD
i-NTD
ii-NTD

Figure 3

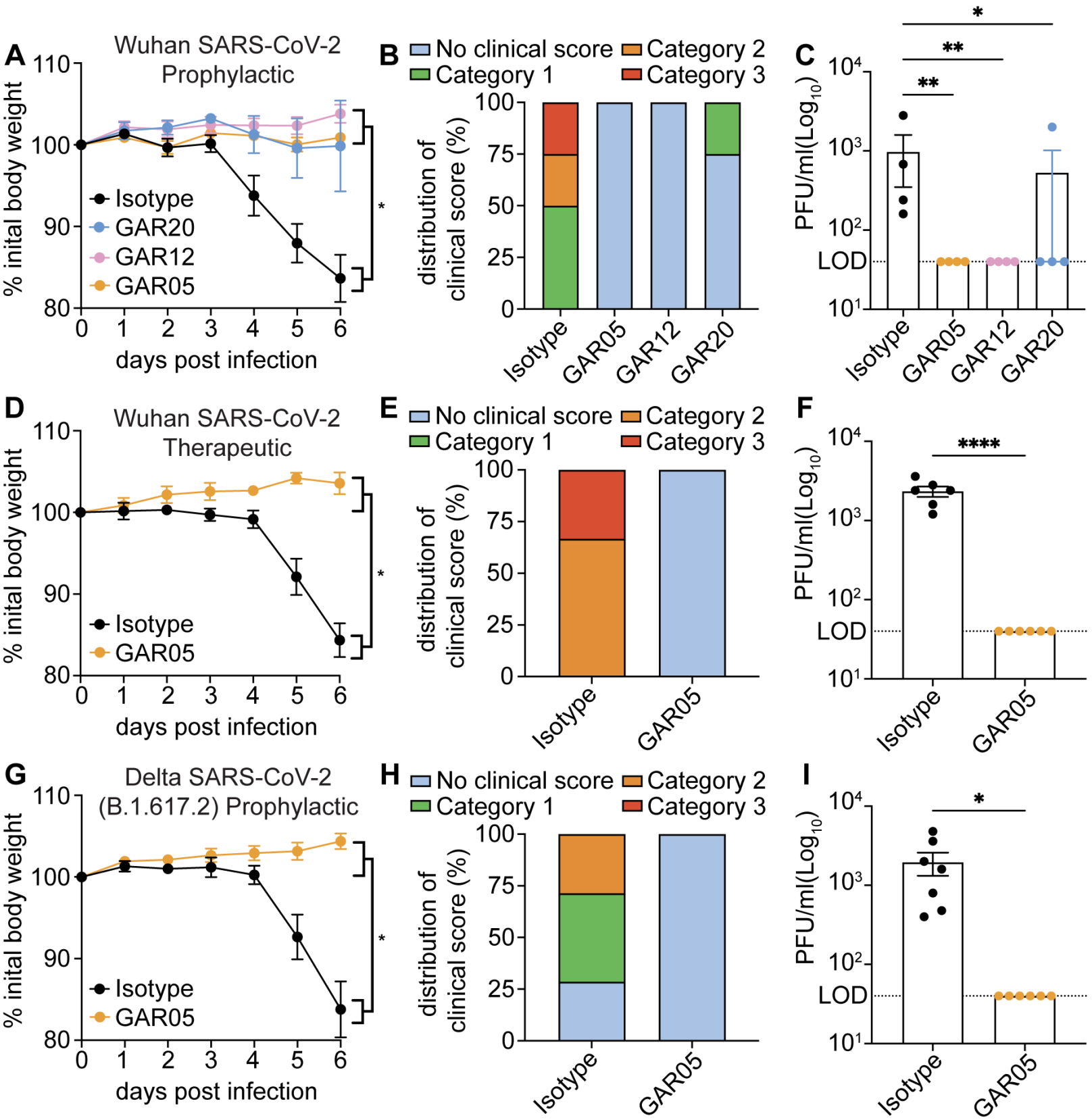
A
Wuhan SARS-CoV-2
Prophylactic
% inital body weight
days post infection
Isotype
GAR20
GAR12
GAR05
B
No clinical score
Category 1
Category 2
Category 3
distribution of clinical score (%)
Isotype
GAR05
GAR12
GAR20
C
PFU/ml(Log10)
LOD
D
Wuhan SARS-CoV-2
Therapeutic
E
F
G
Delta SARS-CoV-2
(B.1.617.2) Prophylactic
H
I

Figure 4

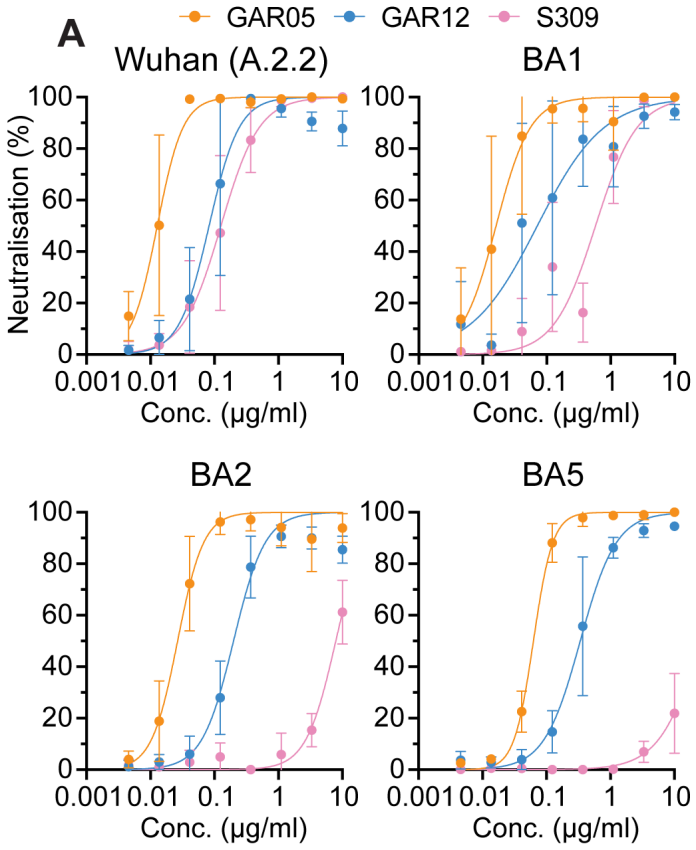

B

IC_{50} (ng/ml)	GAR05	GAR12	S309
A.2.2	82.45	12.77	132.6
BA1	71.31	16.17	804.6
BA2	198.9	26.58	nn
BA5	337.6	62.59	3826

Figure 5